




# Partitioning behavior and lattice misfit of $\gamma/\gamma'$ phases in Ni-based superalloys with different Mo additions

Zhe Ma, Yan-Ling Pei\* , Liang Luo, Lu Qin, Shu-Suo Li, Sheng-Kai Gong

Received: 14 March 2018 / Revised: 1 October 2018 / Accepted: 24 June 2019 / Published online: 13 April 2020  
© The Nonferrous Metals Society of China and Springer-Verlag GmbH Germany, part of Springer Nature 2020

**Abstract** A low-density single crystal (LDS) alloy with the composition of high Mo content was designed. The extra 1.5 wt% Mo was added in the Alloy A with the composition of Ni–6.5Al–8.0Mo–2.4Cr–6.2Ta–4.9Co–1.5Re–(0.01–0.05)Y (wt%) to study the influence of Mo on the lattice parameter and partitioning behavior. Scanning electron microscope (SEM) with energy-dispersive spectrometer (EDS), transmission electron microscopy (TEM) and high-temperature X-ray diffraction (HT-XRD) were used to observe the microstructure, analyze the elemental content and measure the lattice parameter of the alloys. The natural lattice misfit was calculated by lattice constants which were measured by HT-XRD at the temperature from 25 to 1150 °C, and the results showed that the lattice misfit would be more and more negative with temperature increasing. It was found that 1.5 wt% addition of Mo will increase the absolute value of the lattice misfit of  $\gamma/\gamma'$  phases and the volume fraction of  $\gamma'$ , and at the same time, influence the elemental distribution in  $\gamma$  and  $\gamma'$  phases, especially Re and Cr. Re has a higher partitioning ratio ( $k$ ) after the addition of Mo.

**Keywords** Ni-based superalloys; Mo; Lattice misfit; High-temperature X-ray diffraction (HT-XRD); Partitioning behavior

**Electronic supplementary material** The online version of this article (<https://doi.org/10.1007/s12598-019-01309-z>) contains supplementary material, which is available to authorized users.

Z. Ma, Y.-L. Pei\*, L. Luo, L. Qin, S.-S. Li, S.-K. Gong  
School of Materials Science and Engineering, Beihang University, Beijing 100191, China  
e-mail: peiyanling@buaa.edu.cn

## 1 Introduction

Ni-based single crystal (SC) superalloys have been widely used for the production of turbine blade due to their excellent comprehensive service performance [1–3]. New low-density single (LDS) crystal alloys have been developed for turbine blade applications, which have the potential for significant improvements in the thrust-to-weight ratio over current production alloys [4–6]. Mo, instead of some other refractory elements such as W, Re and Ru, has been used as the solid solution strengthener. New low-density SC superalloys have been developed in recent years [7–11]. The density of these two superalloys is about  $8.3 \text{ g}\cdot\text{cm}^{-3}$  while the density of the third-generation superalloy is about  $9.0 \text{ g}\cdot\text{cm}^{-3}$ .

Our research group has developed two kinds of superalloys. The additional 1.5 wt% Mo was added to a Ni-base SC alloy with the composition of Ni–6.5Al–8.0Mo–2.4Cr–6.2Ta–4.9Co–1.5Re–(0.01–0.05)Y (wt%). The base alloy is Alloy A, and the one with higher Mo content is Alloy B. To study the effect of Mo content on the microstructure and stress-rupture properties, creep and stress-rupture tests were conducted by former researchers [12]. Under the test conditions of 850 °C/500 MPa and 1100 °C/130 MPa, it has been found that the addition of 1.5 wt% Mo could achieve lower creep rates and longer stress-rupture lives. On the basis of the former research, the target of this paper is to find out the changes in the microstructure, explain the reason why the addition of Mo can achieve better mechanical properties and try to offer guidance for the next-generation superalloy design.

## 2 Experimental

Two alloys were provided in the experiment. Alloy B has 1.5 wt% higher Mo content than the base Alloy A with the major elements of Ni–Al–Mo–Cr–Co–Ta–Re.

The master alloys were prepared by vacuum induction melting, and then, the SC rods ( $\Phi 15$  mm  $\times$  150 mm) were prepared using a high-rate-solidification (HRS) apparatus with the withdraw rate of 4 mm·min<sup>-1</sup>. The heat treatment for Alloy A is 1300 °C, 2 h + 1305 °C, 2 h + 1310 °C, 6 h + 1315 °C, 6 h, flow air cooling (FAC) + 1080 °C, 2 h, air cooling (AC) + 871 °C, 32 h, AC, and for Alloy B, it is 1290 °C/2 h + 1295 °C/2 h + 1300 °C/6 h + 1305 °C/6 h, FAC + 1080 °C, 2 h, AC + 871 °C, 32 h, AC. Laue back-reflection was adopted to find the [001] direction of the single crystal alloy as the axial direction, and the (100) surface were taken as the exposed surface for the high-temperature X-ray diffraction (HT-XRD) experiment [13–18]. The specimens were cut into 25 mm  $\times$  14 mm  $\times$  2 mm slice block with a 25 mm  $\times$  2 mm  $\times$  1 mm groove where the thermocouple probe can be put into. The samples were measured using a Rigaku SmartLab X-ray diffractometer (XRD) with a heating device at the temperature of 25, 760, 850, 980, 1100 and 1150 °C, respectively. The measurements conditions were 40 kV, 200 mA, scanning rate of 0.6 (°)·min<sup>-1</sup>, heating rate of 20 °C·min<sup>-1</sup>, holding time of 5 min, flowing rate of argon of 0.1 L·min<sup>-1</sup> to prevent the oxidation of samples. The holding time is to ensure that the temperature was stable and the temperature error range was within 5 °C. The separation of XRD peaks could be accomplished by the peak fitting module (PFM) software for origin. Other samples after heat treatment were held at the temperature of 850, 980, 1100 and 1150 °C for 30 min, and water quenching was taken to maintain the microstructure and composition of the alloy at every certain temperature. The microstructure was observed by scanning electron microscope (SEM, APOLLO300). The composition of alloys was determined using a transmission electron microscope (TEM, JEM-2100) equipped with energy-dispersive spectrometer (EDS).

The creep and stress-rupture tests for two alloys were conducted under different test conditions, and the stress-rupture lives are listed in Table 1 [12].

**Table 1** Stress-rupture lives of two alloys under test condition (h)

Alloys	850 °C/500 MPa	980 °C/250 MPa	1100 °C/130 MPa
A	355	95	184
B	440	105	306

## 3 Results and discussion

### 3.1 Effect of Mo content on microstructure of superalloys

The microstructures of the two alloys after full heat treatment were analyzed by former researchers. Water quenching was done to reserve the microstructure and composition of  $\gamma$  and  $\gamma'$  phases. Firstly, the alloys were put into the electric resistance furnace, respectively, at temperatures of 850, 980, 1100 and 1150 °C. In the process of experiment, the scanning time will take about 10 min from 48° to 54° as the scanning speed is 0.6 (°)·min<sup>-1</sup> and it takes about 20 min to keep stable at each testing temperature. The thermal exposure changes the microstructures of the two Ni-based single crystal superalloys. If the duration of the thermal exposure is short and the introduction of the dislocations into the gamma channel is little, the corresponding misfit refers to the constrained misfit. If the duration of the thermal exposure is long enough and the misfit stress is relieved by the introduction of the dislocations, the corresponding misfit refers to the unconstrained misfit. In practice, the durations of the thermal exposure are different and the experimental results are deviated from the exact values of the constrained misfit to some extent. The experimental results in this study are also deviated from the exact values of the constrained misfits, and the extent of the deviation may be different from the conventional study. But the differences of the deviation extents in these two alloys are little and can be neglected when comparing the two alloys in this study. As the specimen would be held at each testing temperature for about 30 min in the HT-XRD test, 30 min was chosen as the temperature holding time before water quenching treatment. The specimens were cut off at least 3 mm from the surface in order to avoid the influence of oxidation layer. The microstructure after water quenching is typically shown in Fig. 1.

Figure 1 shows that as the temperature rises,  $\gamma$  channel will change: Some thinner channel would dissolve and disappear and other thick channels would be thicker; alloying elements may diffuse from  $\gamma'$  to  $\gamma$ , and as a result,  $\gamma'$  phase would be dissolved into  $\gamma$  phase. As Fig. 1 shows, the cubic degree is a little bit higher in Alloy B than Alloy A. The distribution of  $\gamma'$  phase is more homogeneous and stable in Alloy B, especially at high temperatures as Fig. 1a–d shows. In this process, the partitioning behavior was tested. In both alloys, EDS measurements in five different  $\gamma'$  particles and five different positions in the  $\gamma$  matrix were done. At the same time, the fraction of  $\gamma'$  phase of each testing temperatures can be obtained.

The fraction of  $\gamma'$  phase has a significant effect on the mechanical properties of the superalloys, and two methods were adopted to calculate it. Five SEM images of Alloy A

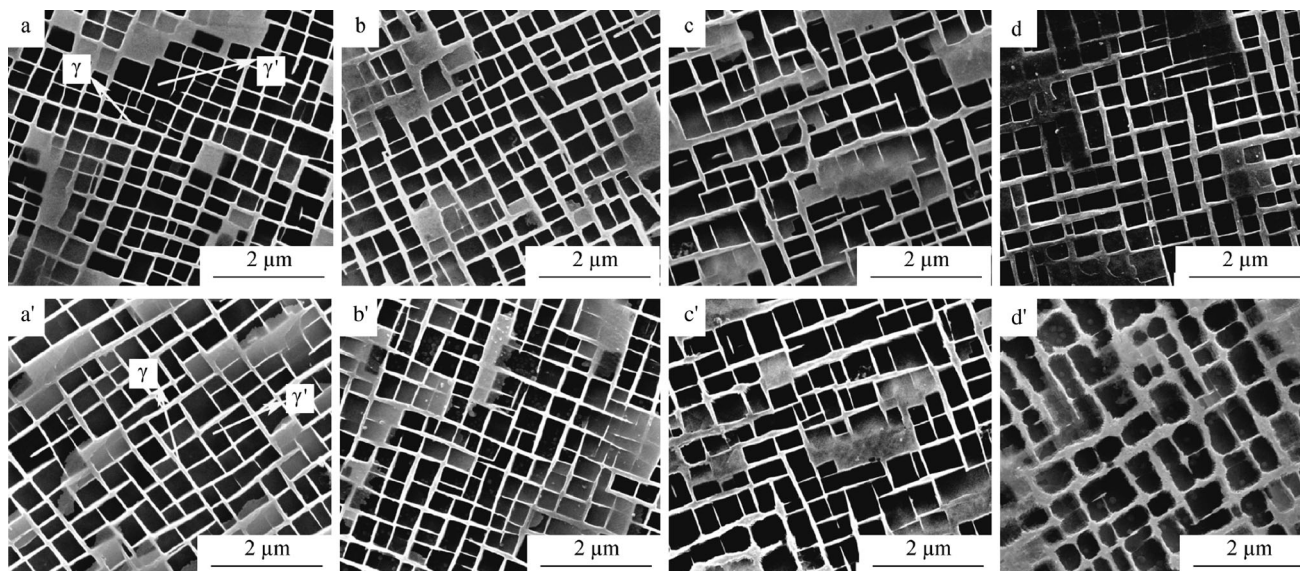


**Fig. 1** OM images of Alloys A and B after quenching at temperatures of a, a' 850 °C, b, b' 980 °C, c, c' 1100 °C and d, d' 1150 °C

and Alloy B (partly shown in Fig. 2) in different positions at each temperature were selected, and then, the average area fraction of the alloys can be gotten by using the Image-Pro software. The determined  $\gamma'$ -area fractions ( $F_{\gamma'}$ ) can be calculated as  $\gamma'$  volume fractions ( $V_{\gamma'}$ ) by: [19, 20]:

$$V_{\gamma'} = \frac{P^3}{P^3 + 3P^2 + 3P + 1} \quad (1)$$

$$P = \frac{F_{\gamma'} + \sqrt{F_{\gamma'}}}{1 - F_{\gamma'}} \quad (2)$$

Volume fraction can be obtained by Eqs. (1) and (2), and the result is shown in Table 2. The other method was using XRD peak separation result, and the peak area integral of  $\gamma$  and  $\gamma'$  represents the volume fraction, as Fig. 2 shows.

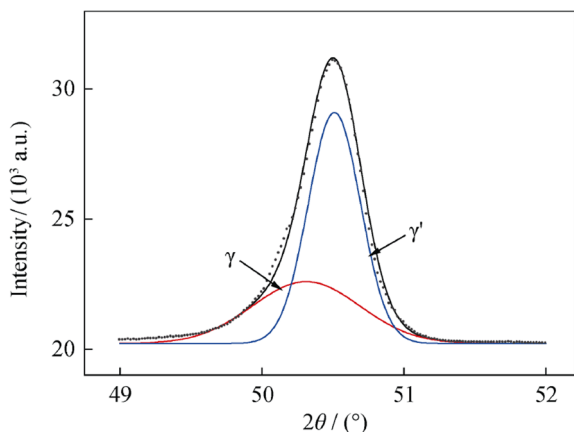


**Fig. 2** Peak separation after XRD of Alloy A at 980 °C

**Table 2** Content of  $\gamma'$  phase in different temperatures of Alloys A and B by two methods (vol%)

Alloys	Methods	25 °C	850 °C	980 °C	1100 °C	1150 °C
A	SEM	64.6	62.6	59.3	55.6	48.3
	XRD	69.1	68.5	64.2	60.3	54.2
B	SEM	65.3	63.5	61.4	58.5	51.2
	XRD	71.0	69.6	66.9	63.3	57.8

Obviously, the volume fraction of  $\gamma'$  phase gradually decreases with the temperature increasing and the trend of the decrease is more obvious when the temperature is above 1100 °C, and it also shows that dissolution rate of  $\gamma'$  phase significantly accelerates above 1100 °C.  $\gamma'$  is a strengthening phase in the superalloys, and it follows the precipitation strengthening mechanism. While the absolute values between the two methods differ significantly, the order of volume fractions is equal. It is reported that proportions of  $\gamma'$ -forming elements such as Al, Ti and Ta should be high, and the  $\gamma'$  fraction is about 70 vol% [1]. It could be seen that Alloy B has higher fraction of  $\gamma'$  at every temperature than Alloy A. Perhaps the reason is that with the 1.5 wt% addition of Mo, the elemental distribution of  $\gamma$  and  $\gamma'$  phases would change a little and some element would diffuse from  $\gamma$  phase to  $\gamma'$  phase, resulting in the increase in  $\gamma'$  volume fraction.

### 3.2 Effect of Mo content on lattice parameter and lattice misfit

Different Mo contents and different temperatures will influence the elemental distribution and lattice parameter of

$\gamma$  and  $\gamma'$  phases in nickel-based superalloys [21–23]. The lattice parameter and lattice misfit of the two phases have a significant effect on the high-temperature mechanical properties. Separation of peaks was used by the Origin PFM software. Two-peak fitting was used. The (200) diffraction peak was fitted. The lattice parameter of  $\gamma$  phase is close to that of  $\gamma'$  so the diffraction peak of the HT-XRD can be separated into two peaks by Origin software. Lattice parameters can be calculated using the Bragg's Law [24]. As  $\gamma'$  phase has a higher volume fraction, the left peak represents  $\gamma$  and the right one is  $\gamma'$ . Figure 2 is the peak separation result of Alloy A at 980 °C, which is an example of the method [25].

From the pattern, the values of  $2\theta$  for  $\gamma$  and  $\gamma'$  phases are 50.312° and 50.510°, and the calculation results for lattice constants are 0.3624 and 0.3610 nm, respectively. Since lattice parameters can be found from the peak separation result as this example shows, the lattice misfits of Alloy A and Alloy B at each testing temperatures can be obtained and the result is shown in Fig. 3.

The results of XRD in Fig. 3 show that  $\gamma$  phase has a larger lattice parameter than  $\gamma'$  phase. Although they have the same fcc structure, compared with the ordered  $\gamma'$  phase, the disordered  $\gamma$  phase has a larger one. In the ordered structure, the interatomic force is stronger so the thermal capacity is smaller so that the displacement due to the lattice vibration is smaller and the coefficient of thermal expansion is also smaller [26]. In a similar way, the  $\gamma$  phase has a larger coefficient of thermal expansion. The lattice parameters of Alloy B are both smaller than those of Alloy A for the  $\gamma$  and  $\gamma'$  phases. Alloy A with a larger volume fraction of  $\gamma'$  has the larger thermal expansion coefficient, so it shows a slightly larger change as the temperature rises.

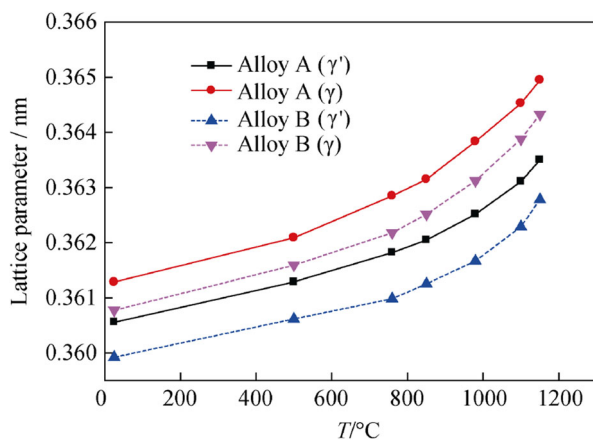


**Fig. 3** Temperature dependence of lattice parameter of  $\gamma$  and  $\gamma'$  phases of Alloys A and B

Lattice misfit is the internal representation of the strained condition and degree of stability of  $\gamma/\gamma'$  coherent interface, which will be influenced by the temperature, composition of the alloying elements and the change of strain state. The so-called natural lattice mismatch is defined as Eq. (3):

$$\delta = 2(a_{\gamma'} - a_{\gamma}) / (a_{\gamma'} + a_{\gamma}) \quad (3)$$

where  $a_{\gamma'}$  and  $a_{\gamma}$  are the free lattice parameters of  $\gamma'$  and  $\gamma$  phase, respectively. Using this formula, lattice misfit of Alloy A and Alloy B at different temperatures can be calculated and the result is shown in Fig. 4.

It can be seen that the lattice misfit of Alloy A and Alloy B at room temperature is negative, which coincides with the result reported [27], and the values are  $-0.202\%$  and  $-0.238\%$ , and it becomes more and more negative as the temperature rises, especially when it comes to high temperature of above 800 °C. What should be noted is that the volume fraction increasing rate of  $\gamma$  is larger than  $\gamma'$ , so that the absolute value of the mismatch would increase with the temperature rising. Alloy B has a more negative lattice misfit than Alloy A at every temperature tested.

### 3.3 Partitioning behavior of alloying elements

The chemical compositions of the two phases were measured by TEM equipped with an EDS system. The TEM samples were taken from the samples held for 30 min at certain temperatures and then water quenching. TEM image of Alloy A at 980 °C was taken as an example, as shown in Fig. 5. It is found that Cr, Co, Re and Mo are partitioned partially to the  $\gamma$  matrix and other elements partitioned approximately equally between  $\gamma$  and  $\gamma'$  phases. The results of EDS agree with measurements from literatures [28].

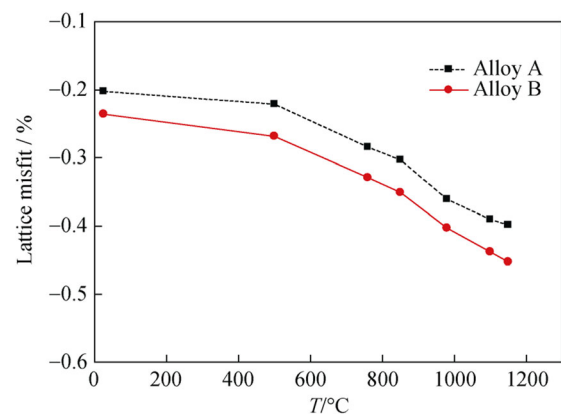


**Fig. 4** Temperature dependence of misfit of  $\gamma$  and  $\gamma'$  phases of Alloys A and B

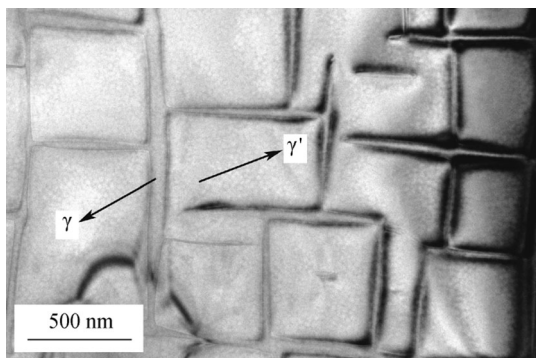


**Fig. 5** TEM image of Alloy A at 980 °C

In order to do more quantitative analysis, detailed elemental content should be tested. As mentioned above, in both alloys, EDS measurements in five different  $\gamma'$  particles and five different positions in the  $\gamma$  matrix were done. Figure 6 shows the concentration of the different alloying elements plotted over the different annealing temperatures in Alloy A and Alloy B for the  $\gamma$  and  $\gamma'$  phases.

The concentration of Ta and Mo in the  $\gamma'$  phase, as shown in Fig. 6, remains rather constant with temperature,

while Co content increases a little. Alloy A is the base alloy, and according to Fig. 6, in  $\gamma$  matrix, the concentration of Re, Cr, Co and Mo decreases with temperature increasing in the investigated alloys. This is easily understandable because at higher temperatures, the  $\gamma'$  phase dissolves and the volume fraction of the  $\gamma$  matrix increases. So, these elements which are mainly enriched in the matrix (see also in Ref. [29]) are distributed in a matrix with larger volume. The amount of Ta in the matrix increases with temperature increasing. As Ta is an element which is enriched in the  $\gamma'$  precipitate phase, an increasing amount is set free into the matrix at higher temperature when the  $\gamma'$  precipitates dissolve. As very lower Al content is observed in specimens annealed at higher temperatures, evaporation of Al during annealing most probably plays a role.

When 1.5 wt% Mo is added, the elemental composition of  $\gamma$  and  $\gamma'$  phases changes as visible in Fig. 6. The content of Mo is obviously higher in the  $\gamma$  matrix, and the dissolution of  $\gamma'$  phase also contributes to the decrease in the concentration of elements initially enriched in the matrix which was mentioned above. Higher Al contents are observed at high temperatures despite the evaporation so it may be inferred that the addition of Mo may lead to the segregation of Al in  $\gamma'$  phase.

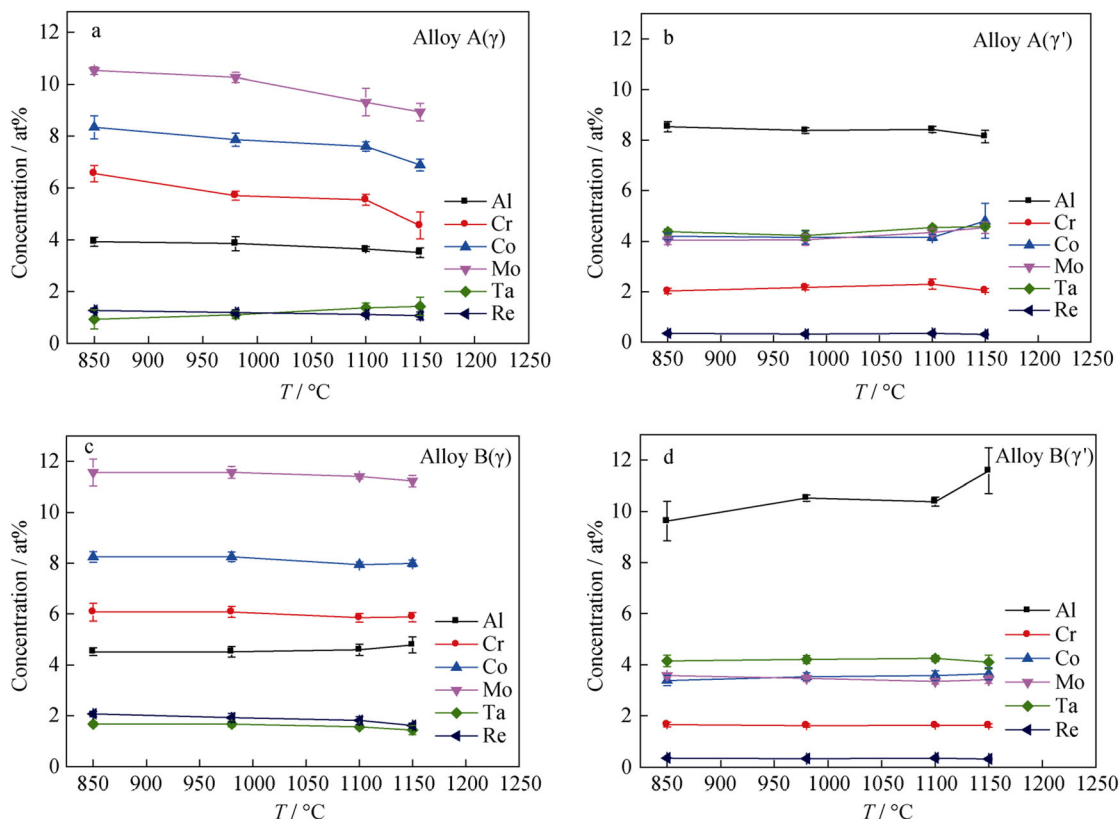


**Fig. 6** Concentration of alloying elements in  $\gamma$  matrix and  $\gamma'$  precipitate phase of Alloys A and B: **a**  $\gamma$  in Alloy A, **b**  $\gamma'$  in Alloy A, **c**  $\gamma$  in Alloy B and **d**  $\gamma'$  in Alloy B

For Re, as visible in Fig. 6, a little increasing concentration is found in the  $\gamma$  phase when 1.5 wt% Mo is added. Under the condition that chemical equilibrium was reached in the specimens, one can deduce that the addition of Mo would cause a higher solubility of Re in the  $\gamma$  phase. At the same time, as the volume fraction of the matrix phase increases at higher temperatures, Re tends to be redistributed from  $\gamma$  matrix to the  $\gamma'$  precipitates. This causes a change in the partitioning ratio of Re in the presence of higher Mo content. Nevertheless, the Re concentration in the  $\gamma'$  precipitates is rather unchanged due to the limitation of the machine's accuracy. And one has to keep in mind that the alloys under investigation here do not precipitate TCP-phases even after prolonged annealing, or in other words they are phase stable as already mentioned above. The addition of Mo changes the solubility of Re in  $\gamma$  matrix and Al in  $\gamma'$  phase.

Elemental partitioning ratios ( $k$ ) were used to show the partitioning behavior of different alloys which are defined as the concentration of an alloying element in the  $\gamma'$  phase ( $C_{\gamma'}$ ) divided by the concentration of the element in the  $\gamma$  matrix ( $C_{\gamma}$ ), as shown in Eq. (4):

$$k = C_{\gamma'} / C_{\gamma} \quad (4)$$

The partitioning of the alloying elements between the matrix and the  $\gamma'$  precipitates can be illustrated by plotting the partitioning ratio ( $k$ ) over temperature as done in Fig. 7.

Smaller values of ( $k$ ) indicate elements enriched in the  $\gamma'$  phase while greater  $k$  values are found for elements enriched in the matrix phase. For Al, Ta ( $k < 1$ ) and Cr, Co and Mo ( $k > 1$ ), the overall behavior is indicated. With temperature increasing, the partitioning of the elements to the respective phase is less pronounced. The  $k$  value of Re changes mostly, while the  $k$  value for Re is larger in Alloy B than in Alloy A. Therefore, partitioning, i.e., a change in

the partitioning behavior of Re in the presence of 1.5 at% Mo addition, is observed here. This partitioning behavior is now found both in the lower temperature range and at higher temperatures. The  $k$  factor of Cr is also bigger in Alloy B than Alloy A, which means that Cr tends to be aggregated from  $\gamma'$  phase to  $\gamma$  matrix as the temperature rises. Mo mainly exists in the  $\gamma$  matrix, and an increased solubility of Re in the  $\gamma$  phase in the presence of more Mo may be the reason why  $k$  factor is larger in the presence of 1.5 wt% Mo addition, which is found at all temperatures.

Although the differences between the two alloys are not significant, it may be inferred that the addition of Mo will influence the partitioning behavior of Re and Cr in  $\gamma$  and  $\gamma'$  phases. In consideration of the accuracy of the experiment, the addition of Mo may also have tiny effect on the partitioning behavior of other alloying elements.

Mo is a solution strengthening element, and the higher Mo contents would decrease the density and cost and obtain proper mechanical properties. In Ni-base SC superalloys, the composition of  $\gamma$  and  $\gamma'$  phases will determine the elemental partitioning ratio, which means the  $k$  factor; the  $k$  factor will influence whether the mismatch is plus or minus and the absolute value, and thus the microstructure of  $\gamma'$  will also be affected [13]. Under different temperatures and stresses, the value of the mismatch would have different effects on coarsening, bonding and rafting of  $\gamma'$  phase, etc., which will finally affect the properties on active service of the superalloys. The addition of Mo and the distribution changes of Re and Cr content may lead to the more negative value of the lattice misfit [30, 31].

Obviously, with Mo addition, the whole distribution of the alloying elements would be more or less influenced and the mechanical properties. The stress-rupture lives of Alloy B are remarkably longer than those of Alloy A, especially

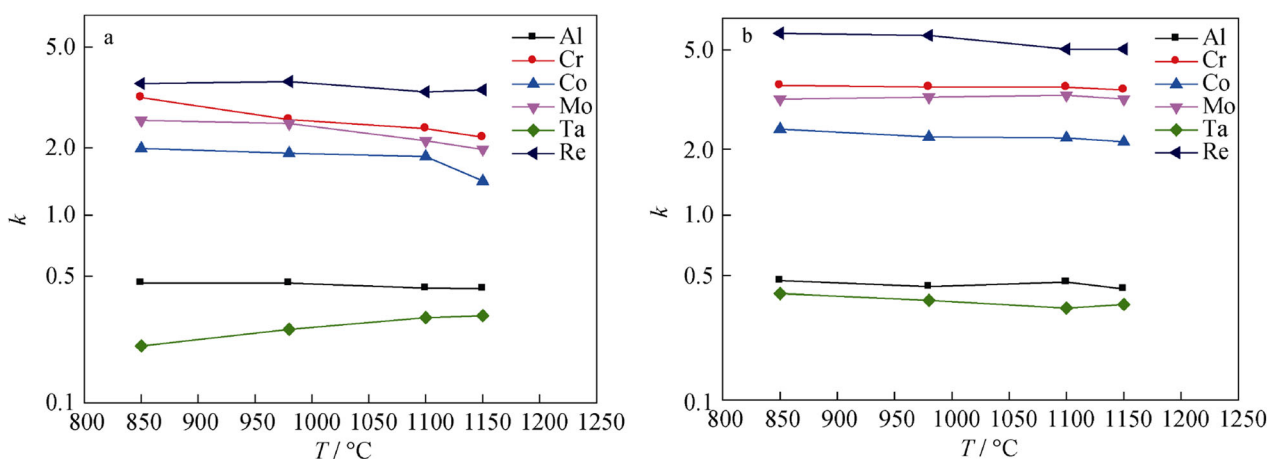


**Fig. 7**  $k$  factor of **a** Alloy A and **b** Alloy B

under the test conditions of 850 °C/500 MPa and 1100 °C/130 MPa, as shown in Table 1. Mo itself plays a role of solution strengthening. The addition of Mo leads to a more negative lattice misfit, and this can be an interfacial strengthening factor. The increasing  $\gamma'$  phase and the high content  $\gamma'$  phase in high temperatures can be a precipitated-phase strengthening factor, and it could be another reason for the increase in the stress-rupture lives. The 1.5 wt% Mo addition has a positive effect on the stress-rupture properties in this work.

#### 4 Conclusion

High-temperature X-ray was used to analyze the lattice parameters of two alloys. The alloy with 1.5 wt% higher Mo content, Alloy B, has a larger absolute value of lattice mismatch in the temperature range of 25–1150 °C and the larger  $\gamma'$  volume fraction than Alloy A at each temperature tested. The chemical composition of  $\gamma$  and  $\gamma'$  phases and the partitioning behavior of alloying elements were determined at high temperatures from 850 °C up to 1150 °C in the two alloys. Owing to the solution strengthening of alloying element, precipitation strengthening of  $\gamma'$  phases and interfacial strengthening effect of  $\gamma/\gamma'$  phases, the mechanical properties of the alloy would increase. While the addition of 1.5 wt% Mo does not alter the partitioning behavior of most alloying elements significantly, it causes partitioning of Al and Re in the alloys investigated here.

**Acknowledgements** This study was financially supported by the National Natural Science Foundation of China (Nos. U1435207, 51371007 and 51671015) and the National Defense Basic Scientific Research Program of China (No. A2120132006).

#### References

- [1] Reed RC. The Superalloys: Fundamentals and Applications. Cambridge: Cambridge University Press; 2006. 112.
- [2] Vattré A, Devincere B, Roos A. Dislocation dynamics simulations of precipitation hardening in Ni-based superalloys with high  $\gamma'$  volume fraction. *Intermetallics*. 2009;17(12):988.
- [3] Liu J, Cao J, Lin X, Song X, Feng J. Microstructure and mechanical properties of diffusion bonded single crystal to polycrystalline Ni-based superalloys joint. *Mater Des*. 2013;49(Complete):622.
- [4] Burns DE, Zhang Y, Teutsch M, Teutsch M, Bade K, Aktaa J, Hemker KJ. Development of Ni-based superalloys for micro-electromechanical systems. *Scr Mater*. 2012;67(5):459.
- [5] Mackay RA, Gabb TP, Garg A. Influence of composition on microstructural parameters of single crystal nickel-base superalloys. *Mater Charact*. 2012;70(Complete):83.
- [6] Zhao HG, Li SS, Pei YL, Gong SK, Xu HB. Microstructure and mechanical properties of Ni<sub>3</sub>Al-based single crystal alloy IC21. *Acta Metall Sin*. 2015;51(10):1279.
- [7] Siebörger D, Brehm H, Wunderlich F, Möller D. Temperature dependence of lattice parameter, misfit and thermal expansion coefficient of matrix,  $\gamma'$  phase and superalloy. *Zeitschrift fuer Metallkunde*. 2001;92(1):58.
- [8] Mukherji D, Gilles R, Barbier B, Genovese DD, Hasse B, Strunz P. Lattice misfit measurement in Inconel 706 containing coherent  $\gamma'$ , and  $\gamma''$  precipitates. *Scr Mater*. 2003;48(4):333.
- [9] Zeman P, Zuzjaková Š, Blažek J, Čerstvý R, Musil J. Thermally activated transformations in metastable alumina coatings prepared by magnetron sputtering. *Surf Coat Technol*. 2014;240:7.
- [10] Hashizume R, Yoshinari A, Kiyono T, Murata Y, Morinaga M. Development of novel Ni-based single crystal superalloys for power-generation gas turbines. *Mater High Temp*. 2007;24(3):163.
- [11] Mackay RA, Gabb TP, Smialek JL, Nathal MV. A new approach of designing superalloys for low density. *J Met*. 2010;62(1):48.
- [12] Liang YF, Li SS, Ai C, Han YF, Gong SK. Effect of Mo content on microstructure and stress-rupture properties of a Ni-base single crystal superalloy. *Prog Nat Sci Mater Int*. 2016;26(1):112.
- [13] Pyczak F, Devrient B, Neuner FC, Mughrabi H. The influence of different alloying elements on the development of the  $\gamma/\gamma'$  microstructure of nickel-base superalloys during high-temperature annealing and deformation. *Acta Mater*. 2005;53(14):3879.
- [14] Siebörger D, Brehm H, Wunderlich F, Möller D, Glatzel U. Temperature dependence of lattice parameter, misfit and thermal expansion coefficient of matrix,  $\gamma'$  phase and superalloy. *Z Metallkd*. 2001;92(1):58.
- [15] Teresiak A, Gebert A, Savyak M, Mattern N, Uhlemann M. In situ high temperature XRD studies of the thermal behaviour of the rapidly quenched Mg77Ni18Y5, alloy under hydrogen. *J Alloy Compd*. 2005;398(1–2):156.
- [16] Huntz AM, Liu C, Kormmeier M, Lebrun JL. The determination of stresses during oxidation of Ni: in situ, measurements by XRD at high temperature. *Corros Sci*. 1993;35(5–8):989.
- [17] Berbenni V, Marini A. Thermoanalytical (TGA-DSC) and high temperature X-ray diffraction (HT-XRD) study of the thermal decomposition processes in Li<sub>2</sub>CO<sub>3</sub>-MnO mixtures. *J Anal Appl Pyrol*. 2002;64(1):43.
- [18] Oezaslan M, Hasché F, Strasser P. In situ observation of bimetallic alloy nanoparticle formation and growth using high-temperature XRD. *Chem Mater*. 2011;23(8):2159.
- [19] Heckl A, Neumeier S, Göken M, Singer RF. The effect of Re and Ru on  $\gamma/\gamma'$  microstructure,  $\gamma$ -solid solution strengthening and creep strength in nickel-base superalloys. *Mater Sci Eng, A*. 2011;528(9):3435.
- [20] Bürgel R. *Handbuch Hochtemperatur-Werkstofftechnik*. Wiesbaden: Vieweg & Sohn; 2006. 24.
- [21] Achary SN, Ambekar BR, Mathews MD, Tyagi AK, Moorthy PN. Study of phase transition and volume thermal expansion in a rare-earth (RE) oxyfluoride system by high-temperature XRD (RE = La, Nd, Sm, Eu and Gd). *Thermochim Acta*. 1998;320(1–2):239.
- [22] Jr MAS, Freitas JCC, Morigaki MK. High-temperature XRD study of thermally induced structural and chemical changes in iron oxide nanoparticles embedded in porous carbons. *J Nanoparticle Res*. 2010;12(8):3097.
- [23] Ohta Y, Yoshizawa H, Nakagawa YG. Microstructural changes in a Ni-base superalloy during service. *Scr Metall*. 1989;23(9):1609.
- [24] Kommel L. Influence of interdiffusion on phases chemical composition and micromechanical properties of the single crystal Ni-base superalloy. *Int Balt Conf Eng Mater Tribol Balttrib*. 2013;35(3):45.
- [25] Tian S, Wang M, Yu H, Xingfu Y, Tang L, Benjiang Q. Influence of element Re on lattice misfits and stress rupture

- properties of single crystal nickel-based superalloys. *Mater Sci Eng, A*. 2010;527(16–17):4458.
- [26] Chieux M, Molins R, Rémy L, Duhamel C, Sennour M, Cadoret Y. Effect of material and environmental parameters on the microstructure evolution and oxidation behavior of a Ni-based superalloy coated with a Pt-modified Ni-aluminide. *Mater Sci Forum*. 2008;595(598):8.
- [27] Mughrabi H. The importance of sign and magnitude of  $\gamma/\gamma'$  lattice misfit in superalloys—with special reference to the new  $\gamma'$ -hardened Co-base superalloys. *Acta Mater*. 2014;81(81):21.
- [28] Murakami H, Honma T, Koizumi Y, Harada H. Distribution of platinum group metals in Ni-base single-crystal superalloys. *Superalloys*. 2000. [https://doi.org/10.7449/2000/superalloys\\_2000\\_747\\_756](https://doi.org/10.7449/2000/superalloys_2000_747_756).
- [29] Volek A, Pyczak F, Singer RF, Mughrabi H. Partitioning of Re between  $\gamma$  and  $\gamma'$  phase in nickel-base superalloys. *Scr Mater*. 2005;52(2):141.
- [30] Mishima Y, Ochiai S, Suzuki T. Lattice parameters of Ni( $\gamma$ ), Ni<sub>3</sub>Al( $\gamma'$ ) and Ni<sub>3</sub>Ga( $\gamma'$ ) solid solutions with additions of transition and B-subgroup elements. *Acta Metall*. 1985;33(6):1161.
- [31] Cao JD, Zhang JS, Hua YQ, Rong Z, Chen RF, Ye YX. High temperature oxidation behavior of Ni-based superalloy GH586 in air. *Rare Met*. 2017;36(11):878.